

# *Chandra* Observation of the $\rho$ Oph Cloud

Kensuke Imanishi, Katsuji Koyama<sup>1</sup>

*Department of Physics, Graduate School of Science, Kyoto University, Sakyo-ku, Kyoto, 606-8502, Japan;*  
*kensuke@cr.scphys.kyoto-u.ac.jp, koyama@cr.scphys.kyoto-u.ac.jp*

and

Yohko Tsuboi

*Department of Astronomy & Astrophysics, 525 Davey Laboratory, Pennsylvania State University, University Park*  
*PA 16802, USA; tsuboi@astro.psu.edu*

## ABSTRACT

We observed a  $17' \times 17'$  region of the  $\rho$  Oph molecular cloud, using the ACIS-I array onboard the *Chandra X-ray Observatory* (CXO). A 100-ks exposure observation revealed  $\sim 100$  X-ray sources above the detection limit of  $\sim 10^{28}$  ergs s<sup>-1</sup>. About 2/3 of the X-ray sources are identified with an optical and/or infrared counterpart, including significant numbers of Class I, II and III sources and a few brown dwarfs. The X-ray detection rate of Class I sources is a surprisingly high 70 %. Many X-ray flares, possibly due to the magnetic activity, are found from all of the classes. We make systematic spectral studies of the quiescent and flare X-rays for all the X-ray sources. The X-ray temperatures and absorptions of Class I sources are generally larger than those of Class II and III sources. Also X-ray flares from Class I sources show slightly higher duty ratio, temperature, and luminosity, than those of more evolved classes. We further give brief results on brown dwarfs, sources in a younger phase than Class I, unclassified, and unidentified sources. Details for several selected young stellar objects, including the first detection of a neutral iron line (6.4 keV) from a Class I source (YLW 16A), are separately addressed.

---

<sup>1</sup>CREST, Japan Science and Technology Corporation (JST), 4-1-8 Honmachi, Kawaguchi, Saitama, 332-0012, Japan

## 1. INTRODUCTION

Evolution of low-mass young stellar objects (YSOs) can be traced by the infrared – sub *mm* radio spectral energy distributions (SEDs): molecular cloud cores through protostars are represented by Class 0 and Class I SEDs, while classical T Tauri stars (CTTSs) and weak-line T Tauri stars (WTTSs) exhibit Class II and Class III SEDs (Shu, Adams, & Lizano 1987; André & Montmerle 1994). With the *Einstein* satellite, T Tauri stars (TTSs = CTTSs and WTTSs) have been found to emit soft X-rays, with the X-ray characteristics of moderate plasma temperature ( $\sim 1$  keV), strong variability and occasional rapid flares. These are consistent with the scenario of enhanced solar-type activity, attributable to magnetic dynamo processes (Feigelson & DeCampli 1981; Montmerle et al. 1983).

Protostars are often embedded deeply in star forming clouds, shrouded by dense circumstellar gas and dust, hence generally invisible in the optical, near infrared and even soft X-ray bands. X-rays from Class I sources (the late phase of protostars) have been reported in deep *ASCA* and *ROSAT* images of the  $\rho$  Ophiuchi cloud (Koyama et al. 1994; Casanova et al. 1995; Kamata et al. 1997; Grosso et al. 1997; Carkner, Kozak, & Feigelson 1998; Tsuboi 1999; Tsuboi et al. 2000; Grosso et al. 2000; Grosso 2001). However possible contamination from nearby TTSs (or others) would not be removed with the limited spatial resolution of *ASCA*. Very low count rates from *ROSAT* hampered quantitative X-ray study on these Class I sources. In order to shed light on the embedded YSOs, like Class I sources in the  $\rho$  Ophiuchi cloud, we have observed this cloud with the *Chandra X-ray Observatory* (CXO, Weisskopf, O’deh, & van Speybroeck 1997), which has wide energy band sensitivity coupled with unprecedented spatial resolution.

In this paper, we systematically study the X-ray features of the young stellar objects in the  $\rho$  Ophiuchi cloud based on the *Chandra* results. For this purpose, we first clarify our criteria of source classifications based on the near- to far-IR data. Class I sources are selected from near- to mid-IR band or near- to far-IR band spectra (André & Montmerle 1994; Casanova et al. 1995; Chen et al. 1995; Chen et al. 1997; Motte, André, & Neri 1998; Luhman & Rieke 1999; Grosso et al. 2000). Since the classifications of these papers are not fully consistent with each other, we regard a bonafide Class I source (Class I, here and after) if it is re-

ferred to as a Class I source by all the papers, and the others to be Class I candidates (Class I<sub>c</sub>, here and after). Class II and III sources (here Class II and Class III) are simply selected by the spectral index between near- and mid- IR bands (André & Montmerle 1994; Casanova et al. 1995; Luhman & Rieke 1999; Grosso et al. 2000). The age or evolution sequence of Class I<sub>c</sub> should be in between Class I and Class II. We also use the terminology “Class I+I<sub>c</sub>” by combining the Class I and Class I<sub>c</sub> for simplicity. Likewise, “Class II+III” means a combined group of Class II and Class III. A brown dwarf (here and after, BD) means a star with mass falling well below the hydrogen-burning limit of  $0.08 M_{\odot}$ , and a brown dwarf candidate (here and after, BD<sub>c</sub>) indicates a star with mass close to  $0.08 M_{\odot}$  (Wilking, Greene, & Meyer 1999; Cushing, Tokunaga, & Kobayashi 2000).

For comparison with the previous X-ray and infrared results, we assume the distance to the  $\rho$  Oph region to be 165 pc (Dame et al. 1987) throughout this paper, although *Hipparcos* data suggest a closer distance of  $\sim 120$  pc (Knude & Hog 1998).

## 2. OBSERVATION AND DATA REDUCTION

The observation was made on 2000 April 13–14 with the ACIS-I array consisting of four abutted X-ray CCDs, which covered a field including the southeast part of the  $\rho$  Oph cloud in the 0.2–10 keV band. The telescope optical axis position on the ACIS-I array is R.A. =  $16^{\text{h}}27^{\text{m}}18.1^{\text{s}}$ , Dec =  $-24^{\circ}34'21.9''$  (epoch 2000). We use Level 1 processed events provided by the pipeline processing at the Chandra X-ray Center. The total available exposure time is  $\approx 10^2$  ks. To minimize the effect of the degradation of charge transfer inefficiency (CTI), we apply the improved data processing technique developed by Townsley et al. (2000). To reject background events, we apply a grade filter to keep only *ASCA* grades<sup>2</sup> 0, 2, 3, 4, and 6.

## 3. ANALYSIS AND RESULTS

### 3.1. Source Detection

Figure 1 shows the ACIS-I false-color image of the  $\rho$  Oph cloud. Red and blue colors represent photons in the soft (0.7–2.0 keV) and hard (2.0–7.0 keV) X-ray bands, respectively. For source finding, we run the

---

<sup>2</sup>see <http://asc.harvard.edu/udocs/docs/POG/MPOG/index.html>

program *wavdetect*<sup>3</sup> in the total (0.5–9.0 keV) X-ray band. We set the significance criterion at  $10^{-7}$  and wavelet scales ranging from 1 to 16 pixels in multiples of  $\sqrt{2}$ . In the  $17'.4 \times 17'.4$  field, we detected 87 sources with a confidence level of  $\gtrsim 5.3 \sigma$ . The source position and ACIS-I count rate for each source are listed in Table 1 (columns 2–5), where the X-ray photons are extracted from  $1''.5$ – $22''.7$  radius circles, depending on the angular distance from the optical axis of the telescope.

### 3.2. Source Classification

We searched for a near-infrared counterpart from the three-color (*JHK*) imaging survey by Barsony et al. (1997), and find that 2/3 (58) of the X-ray sources have a counterpart (column 2 in Table 2). The other 1/3 (29) have no counterpart (here and after, unidentified sources), most of which are blue (hard X-ray sources) in Figure 1. Using the criteria given in §1, we find 7 Class Is and 11 Class I<sub>c</sub>s; most of them appeared blue in Figure 1, or mainly emit hard X-ray photons. We also find 1 BD and 1 BD<sub>c</sub> (No.76 and No.81), and at least 1 foreground star (No.52, Festin 1998). The other 37 sources are mainly colored red, hence are soft band sources, of which 20 are classified as Class II+IIIs, and 17 are unclassified yet (here and after, unclassified sources).

We also search for counterparts in the previous X-ray surveys with *ROSAT* PSPC (Casanova et al. 1995), *ROSAT* HRI (Grosso et al. 2000; Grosso 2001), and *ASCA* (Kamata et al. 1997; Tsuboi et al. 2000), and find only 22 sources in these surveys (columns 3–5 in Table 2). In contrast, while most PSPC and *ASCA* sources are found in the table, about 10 HRI sources in our field of view are not detected, although the typical HRI luminosity of  $10^{30}$  ergs s<sup>-1</sup> is well above our detection limit of  $\sim 10^{28}$  ergs s<sup>-1</sup> (see §4). The results of the classifications and identifications are summarized in Table 2.

### 3.3. Timing Analysis and Flares

For all the X-ray sources, we make light curves in the total X-ray band. We define a flare by following two criteria: (1) a constant flux hypothesis for the light curve is rejected with a chi-square fitting, and (2) the X-ray flux increases and/or decreases by more than double the preceding/following flux with a time

scale smaller than a few  $10^4$  sec.

We then pick up 7, 7, 12, 9, and 1 flares from 7 class Is, 11 Class I<sub>c</sub>s, 20 Class II+IIIs, 17 unclassified sources, and 29 unidentified sources, respectively. For example, the flare light curves of Class I+I<sub>c</sub>s are given in Figure 2. A Class I source YLW 16A (No.57) exhibited a giant flare, in which a significant fraction of X-ray photons pile up (more than two X-ray photons register in a single ACIS pixel within one read-out cycle). Hence the light curve of YLW 16A in Figure 2 is extracted from a  $2''.5$ – $7''.5$  annulus in order to avoid the pile-up effect. Except for this giant flare, most of the other flares show a typical profile which is found in more evolved Class II and IIIs: a fast rise and slow decay.

### 3.4. X-ray Spectra and Luminosities

We make and analyze the X-ray spectra of all the detected X-ray sources. For the flare sources, we treat the spectra in quiescent and flare phases separately. Flare phase is defined as the time from  $(t_p - t_r)$  to  $(t_p + t_d)$ , where  $t_p$ ,  $t_r$ , and  $t_d$  are epoch of the flare peak and  $e$ -folding time for the rising and decaying phases, respectively. From all the source spectra, we subtract a common background spectrum which is made from a source-free 63 arcmin<sup>2</sup> region in the ACIS-I field. We then fit the spectra with a thin thermal plasma model. The metal abundance is well determined only for bright sources to be around 0.3 solar, which is consistent with the previous *ASCA* results (Koyama et al. 1994; Kamata et al. 1997). We therefore fix the abundance to 0.3 solar unless otherwise noted, because photon statistics are generally limited. The free parameters are plasma temperature ( $kT$ ), emission measure (EM), and absorption column ( $N_H$ ). If the temperature is not constrained, which is often the case for very faint sources, we fix the temperature at two representative values of 1 keV (soft source) and 5 keV (hard source), and estimate respective absorptions and luminosities. These spectral fits are generally acceptable except WL 22 (No.10), YLW 16A (No.57), and ROXs 21 (No.40), which are treated separately in §4.8. The best-fit temperature, emission measure, absorption column density, flux, and absorption-corrected luminosity in 0.5–10 keV are listed in Table 1 (columns 6–10).

Since the *ASCA* results are available for some of the bright ACIS sources, we cross-check the best-fit parameters and find good agreement between the two within the statistical errors. We are therefore con-

<sup>3</sup>see <http://asc.harvard.edu/udocs/docs/swdocs/detect/html/>

fidant with the ACIS-I spectral fitting even in the rather early phase of the *Chandra* mission.

## 4. DISCUSSION

### 4.1. X-rays from Protostars

In the ACIS-I field, 10 Class Is and 16 Class I<sub>c</sub>s have been reported with near- to far-IR observations. Among them, we detect X-rays from 7 Class Is and 11 Class I<sub>c</sub>s above the detection limit of  $\sim 10^{28}$  ergs s<sup>-1</sup>. Thus the X-ray detection rates are as high as 70 % in both Class Is and Class I<sub>c</sub>s. The lack of X-rays from the other Class I+I<sub>c</sub>s could be partly due to short time variability. For example, WL 21 (No 8) and YLW 16B (No.60) are hardly visible, except when they exhibit an X-ray flare (see Figure 2a and 2j). Also long-term variability, like the 11-year cycle of solar activity, may not be ignored. We hence suspect that all the Class I+I<sub>c</sub>s, at least those in the  $\rho$  Oph cloud, are potential X-ray sources. Carkner, Kozak, & Feigelson (1998) compiled the X-ray emission from YSOs using *ROSAT* PSPC and reported that the X-ray detection rate from Class I+I<sub>c</sub>s was only  $\sim 10\%$  above the detection limit of  $10^{29}$  ergs s<sup>-1</sup>. Our high detection rate of Class I+I<sub>c</sub>s ( $\sim 70\%$ ) is due to the higher sensitivity of *Chandra*, especially in the hard X-ray band. In fact, if we convert the *Chandra* flux of the 18 Class I+I<sub>c</sub>s to the PSPC counts using the *pimms* software<sup>4</sup>, we find only 4 sources fall above the PSPC lower limit ( $\approx 10^{-3}$  cts s<sup>-1</sup>), even in their flare phases. This corresponds to the PSPC detection rate of  $\sim 20\%$ .

To search for X-rays from an even younger phase than Class I, we check hard X-ray enhancements from 41 starless cores (Motte, André, & Neri 1998) in the ACIS-I field. The 3–8 keV band photon fluxes in a 13'' radius circle around the 1300  $\mu$ m sources are either below the 3  $\sigma$  significance level (37 sources) or are contaminated by nearby YSOs (4 sources).

### 4.2. X-rays from Brown Dwarfs

In our field of view, 3 BDs and 4 BD<sub>c</sub>s have been reported with infrared spectroscopy (Wilking, Greene, & Meyer 1999; Cushing, Tokunaga, & Kobayashi 2000). We detect X-rays from 1 BD (GY 310, No.76) and 1 BD<sub>c</sub> (GY 326, No.81). We should note that *ROSAT* also found X-rays from another BD GY 202 (Neuhäuser et al. 1999). The ages of these stars are

estimated to be in the range of  $(0.1-5)\times 10^6$  yr (Wilking, Greene, & Meyer 1999; Cushing, Tokunaga, & Kobayashi 2000). Interestingly, the other non-X-ray BDs and BD<sub>c</sub>s have systematically older ages of  $(2-90)\times 10^6$  yr. The X-ray properties of the BD and BD<sub>c</sub> are similar to Class II+III<sub>s</sub>: relatively low absorption ( $0.5-2.3\times 10^{22}$  cm<sup>-3</sup>) and temperature (0.9–2.0 keV). Both have  $L_X/L_{\text{bol}}$  of about  $3\times 10^{-4}$ , like typical low mass YSOs. Although the X-rays show aperiodic variability, no flare-like event is found.

### 4.3. $N_{\text{H}}$ and $(J - H)$

Using the  $J$  and  $H$  band magnitudes of Barsony et al. (1997), we display the relation between the X-ray absorption column ( $N_{\text{H}}$ ) and the IR color ( $J - H$ ) in Figure 3. From this figure, we see that  $N_{\text{H}}$  is roughly proportional to  $(J - H)$ . The best-fit linear relation is  $(N_{\text{H}}/10^{22}\text{cm}^{-2}) = (1.26\pm 0.08)\{(J - H) + (0.65\pm 0.09)\}$ , where the data points of No.1, 8, 23, and 77 are excluded for the fitting (see the next paragraph). The offset of 0.65 mag corresponds to that of the zero-reddening K-M type stars (Cox 2000). Using the relation of  $A_{\text{v}}$  and infrared extinction of the  $\rho$  Oph cloud (Martin & Whittet 1990), we obtain a relation of  $N_{\text{H}} [\text{cm}^{-2}] = (1.59\pm 0.40)\times 10^{21} A_{\text{v}}$ , which should be compared to  $N_{\text{H}} [\text{cm}^{-2}] = 1.79\times 10^{21} A_{\text{v}}$  in the interstellar space of our Galaxy (Predehl & Schmitt 1995).

Large  $N_{\text{H}}$  excesses are found in 3 Class I+I<sub>c</sub>s: WL 12 (No.1), WL 21 (No 8), and EL 29 (No.23). Since the X-rays would be emitted from the stellar surface or innermost disk, these Class I+I<sub>c</sub>s should have extra infrared photons coming from outer regions. One possibility is that IR photons from the stellar surface escape above or below the accretion disk or torus, then the envelope gas scatters the IR photons into our line of sight. Since the scattering efficiency is larger at shorter wavelengths, this process makes apparent  $(J - H)$  smaller than that expected from  $N_{\text{H}}$ .

An unclassified source, GY 312 (No.77) also shows large  $N_{\text{H}}$  excess. The X-ray properties of this source, high  $kT$ ,  $N_{\text{H}}$ , magnetic field, and  $L_X(\text{flare})/L_X(\text{quiescent})$  are more similar to Class Is than Class II+III<sub>s</sub> (see also figures 4, 6, and 7), hence GY 312 may be a Class I.

### 4.4. $N_{\text{H}}$ and $kT$

We display the relation between absorption ( $N_{\text{H}}$ ) and temperature ( $kT$ ) in Figure 4. For flare sources,

<sup>4</sup>See <http://asc.harvard.edu/toolkit/pimms.jsp>

data points in the quiescent and flare phases are separately plotted. The data are limited to bright sources, for which both  $N_{\text{H}}$  and  $kT$  are well constrained. ROX s21 (No.40) is excluded because this shows a complicated spectrum (see §4.8.6). From Figure 4, we see that  $N_{\text{H}}$  values for class I+I<sub>c</sub>s are larger than those of Class II+III<sub>s</sub>. This supports the idea that the X-rays from Class I+I<sub>c</sub>s come through denser envelopes surrounding the protostars.

We also see that the temperatures of Class I+I<sub>c</sub>s are systematically larger than those of Class II+III<sub>s</sub> both in quiescent and flare phases. This result confirms and further extends the early *ASCA* results (Koyama et al. 1994; Kamata et al. 1997).

#### 4.5. $L_X$ and $L_{\text{bol}}$

For sources whose bolometric luminosity is well determined, we display the luminosity relation between the X-ray ( $L_X$ ) and the bolometric ( $L_{\text{bol}}$ ) in Figure 5, then fit the data with a linear function. The best-fit  $L_X/L_{\text{bol}}$  values in quiescent phases are  $4.4 \times 10^{-5}$  and  $4.3 \times 10^{-4}$  for Class I+I<sub>c</sub>s and Class II+III<sub>s</sub>, respectively, while those in flare phases are  $8.8 \times 10^{-4}$  (Class I+I<sub>c</sub>s) and  $1.7 \times 10^{-3}$  (Class II+III<sub>s</sub>). We thus confirm the  $L_X/L_{\text{bol}} \sim 10^{-4}$  relation for quiescent phases of Class II+III<sub>s</sub> (Feigelson et al. 1993; Casanova et al. 1995; Grosso et al. 2000). Class I+I<sub>c</sub>s, on the other hand, show significantly lower  $L_X/L_{\text{bol}}$  values in both the flare and quiescent phases than those of Class II+III<sub>s</sub>. This can be interpreted that most of  $L_{\text{bol}}$  of Class I+I<sub>c</sub>s comes from accreting matter rather than the stellar surface, because these objects are in a dynamical mass-accretion phase.

We also see that the X-ray luminosities of 7 flares and 4 quiescent phases well exceed the saturation limit ( $\sim 10^{-3}$ ) seen in low-mass main-sequence stars (Fleming, Schmitt, & Giampapa 1995). This supports the idea that X-ray emitting regions are larger than the stellar surface, which is consistent with the star-disk arcade scenario (Montmerle et al. 2000).

#### 4.6. X-ray flares, $L_X$ , $kT$ and EM relation

We have detected a number of flares, which leads us to a systematic study. The duty ratios of flares, 14, 12, and 9 flares from 18 Class I+I<sub>c</sub>s, 20 Class II+III<sub>s</sub>, and 17 unclassified sources, are nearly equal among these classes, although a hint of larger flare rate is seen in younger phase, Class I+I<sub>c</sub>s. Regardless of the IR classes, most of the flares show typical characteristics

of stellar flares: a fast rise and slow decay in flux and temperature.

We plot the luminosity ( $L_X$ ) correlation between flare and quiescent phases in Figure 6. We see that  $L_X$  in quiescent phases is largely scattered from  $2 \times 10^{28}$  to  $5 \times 10^{30}$  ergs s<sup>-1</sup>, irrespective of the IR classes, while  $L_X(\text{flare})/L_X(\text{quiescent})$  of Class I+I<sub>c</sub>s is systematically larger than that of Class II+III<sub>s</sub>.

We then make the correlation map between  $kT$  and emission measure (EM) of flare phases in Figure 7. Feldman, Laming, & Doschek (1995) found a universal correlation between the temperature and emission measure ranging from solar to stellar flares. Shibata & Yokoyama (1999) confirmed the observational correlation by compiling the data of Feldman, Laming, & Doschek (1995), solar micro flares (Shimizu 1995), a T Tauri flare (Tsuboi et al. 1998), and a protostellar flare (Koyama et al. 1996). They further derived a relation of  $\text{EM} \propto B^{-5} T^{17/2}$ , which is given by dashed lines in Figure 7 for the magnetic fields of 15, 50, and 150 Gauss.

The data of YSOs, solar flares, and solar micro flares globally follow the relation along the constant magnetic field (15–150 G) line, in spite of large difference of  $kT$  and EM between these objects. In detail, we find a hint that the magnetic fields in the flares for class I+I<sub>c</sub>s (50–150 G) are systematically larger than those for class II+III<sub>s</sub> (15–50 G). This implies that the magnetic fields in flares may become smaller as a star evolves.

#### 4.7. Comments on the Unidentified Sources

In Table 1, we find that the absorptions and temperatures of most of the 29 unidentified sources are larger than those of Class II+III<sub>s</sub>. To increase statistics, we co-add all the unidentified sources to make a composite spectrum and fit it with a power-law model. The best-fit photon index is  $1.6_{-0.2}^{+0.3}$ , which is similar to that of the canonical value of AGNs ( $\sim 1.7$ ). The best-fit  $N_{\text{H}}$  value is  $5.9_{-1.1}^{+1.3} \times 10^{22}$  cm<sup>-2</sup>, nearly equal to the average value through this dark cloud (Tachihara, Mizuno, & Fukui 2000). Inversely, if the background sources have a mean photon index of 1.6 and are absorbed by the cloud gas of  $N_{\text{H}} = 5.9 \times 10^{22}$  cm<sup>-2</sup>, the log  $N - \log S$  relation by Mushotzky et al. (2000) predicts the detectable source numbers to be a few tens. Thus most of the unidentified sources are likely to be background AGNs, although some fraction may be cloud members and/or foreground

sources with a small bolometric luminosity. The latter is likely very low mass YSOs such as BDs. No.30 would be a good candidate for the latter case, because it exhibits a rapid flare with similar temperature and absorption to those of Class I+I<sub>c</sub>s.

#### 4.8. Individual Sources

Further details of selected 6 Class I+ I<sub>c</sub> and 1 Class III sources are given below.

##### 4.8.1. WL 22 (No.10)

The X-ray spectrum of WL 22 exhibits clear line structure at  $\sim 3.2$  and  $\sim 3.9$  keV as shown in Figure 8. The line energies correspond to He-like Ca and Ar. We hence relax the abundances of these elements to be free and fit with a thin thermal model. The best-fit  $kT$  and  $N_{\text{H}}$  are  $2.7_{-1.0}^{+2.5}$  keV and  $13.9_{-5.5}^{+18.8} \times 10^{22}$  cm<sup>-2</sup>, respectively (Table 1), while the abundances of Ar and Ca are  $9.3_{-8.3}^{+15.0}$  and  $12.0_{-8.1}^{+14.1}$  of solar. Thus Ca is extremely overabundant, although the mechanism is an open question.

##### 4.8.2. EL 29 (No.23)

EL 29 exhibits an X-ray flare with an  $e$ -folding time of  $\sim 10$  ks (Figure 2b). The average temperature and flux in the flare are 7.5 keV and  $5.1 \times 10^{30}$  ergs s<sup>-1</sup>, while those in the quiescent phase are 4.3 keV and  $2.0 \times 10^{30}$  ergs s<sup>-1</sup>, respectively (Table 1). The *ASCA* satellite visited EL 29 twice with respective exposure times of 40 and 100 ks. In the first observation it exhibited an X-ray flare similar to the present observation (Kamata et al. 1997). It became however quiescent at  $3 \times 10^{30}$  ergs s<sup>-1</sup> in the second observation (Tsuboi et al. 2000). Hence we infer that EL 29 shows quiescent luminosity of  $\sim 10^{30}$  ergs s<sup>-1</sup>, and exhibits frequent X-ray flares.

##### 4.8.3. WL 6 (No.44) and GY 256 (No.45)

Kamata et al. (1997) claimed the detection of hard X-rays from WL 6 with *ASCA*, although the nearby source GY 256, another Class I source, may contaminate the spectrum. The X-ray light curve showed a sinusoidal shape of about 20 hour period. Since they found no temperature variation, which is usually associated with a normal flare, they claimed that the modulation is due to stellar rotations. In the present observation, we clearly detect hard X-rays not only from WL 6 but also from GY 256. Two faint flares are found from GY 256, with higher temperature than

the quiescent phase (Table 1 and Fig. 2g). However no sinusoidal light curve is noted from WL 6 nor from GY 256.

##### 4.8.4. YLW 15A (No.54)

*ROSAT* HRI detected an extraordinary X-ray flare from YLW 15A (Grosso et al. 1997). The inferred luminosity, however, depends largely on the assumed spectrum. We therefore re-estimate the luminosity using our best-fit temperature (4.9 keV) and  $N_{\text{H}}$  ( $4.4 \times 10^{22}$  cm<sup>-2</sup>) for a flare (Table 1). The HRI count rate at the flare peak of  $\sim 17$  cts ks<sup>-1</sup> is then converted to the peak luminosity of  $10^{33}$  ergs s<sup>-1</sup>, which is  $\sim 6$  times brighter than that of the brightest flare seen in YLW 16A (see §4.8.5), but may not be extraordinary. Subsequent *ASCA* observation discovered three quasi-periodic X-ray flares with an interval of  $\sim 20$  hours (Tsuboi et al. 2000). These flares are interpreted with a star-disk arcade conjecture (Montmerle et al. 2000), with an X-ray emission mechanism somehow different from that of Class II+IIIs which may have magnetic arcades within the star. Although *Chandra* confirms the hard X-ray emission and finds a typical flare from YLW 15A (Fig. 2h), no multiple-flares are found. Thus quasi-periodic flares are not always present but rather occasional phenomena.

##### 4.8.5. YLW 16A (No.57)

The light curve of YLW 16A seems to be comprised of 2 flares; the first is rather complex with several spike-like structures and the second is a giant flare of unusual profile (Figure 9, left panel). We examine the spectral evolution by slicing the data in time as shown in Figure 9 (left panel). In phases 7–9, we extract the spectra from the same region (a  $2''.5$ – $7''.5$  radius annulus) as the light curve data, because these phases suffer from the pile-up effect (see §3.3). We first fit the spectra with a thin thermal model allowing the abundance and  $N_{\text{H}}$  to be free for all the phases, and find no significant variation from phase to phase both in abundance ( $\cong 0.3$  solar) and  $N_{\text{H}}$ . We hence fix the abundance to be 0.3 solar and fit the spectra assuming that  $N_{\text{H}}$  is consistent in all the phases. The best-fit parameters for each time interval are shown in Table 3. As seen in Figure 9 (left panel), the temperature ( $kT$ ) and emission measure (EM) increase from phase 2 and reach peak values in phase 3, then gradually decrease. The peak luminosity is estimated to be  $1.3 \times 10^{31}$  ergs s<sup>-1</sup>. These phenomena of the first

flare are similar to other flares found in Class I+I<sub>c</sub>s and Class II+III<sub>s</sub>.

The second flare shows unusual time profiles in the flux and emission measure (EM). However, the temperature profile is more typical of the normal flare; at phase 7 it increases rapidly, and nearly stays constant or shows gradual decay. These profiles may be understood by the partial occultation of a flare due to the stellar rotations. We hence fit the light curve of the second flare with a model of exponential (flare)  $\times$  sinusoidal (rotation modulation) function, and obtain the rotation period of  $\sim 34$  hours.

Figure 9 (right panel) is the spectrum during the large flare. A remarkable finding is an additional emission line feature near the 6.7 keV line of highly ionized iron. The best fit line energy is  $6.4_{-0.4}^{+0.1}$  keV, which is attributable to neutral or low ionized iron. The most plausible origin is fluorescence from cold iron in the circumstellar gas. If the circumstellar gas is spherically distributed around the X-ray source, the equivalent width of iron is estimated to be  $\approx 10 Z_{\text{Fe}}(N_{\text{H}}/10^{22} \text{ cm}^{-2}) \text{ eV}$ , where  $Z_{\text{Fe}}$  and  $N_{\text{H}}$  are the abundance of iron and column density, respectively (Inoue 1985). Since the observed column density of  $4.7 \times 10^{22} \text{ cm}^{-2}$  includes the interstellar gas, that of circumstellar gas should be less than this value. Using the iron abundance of 0.3 solar, we predict the maximum equivalent width to be  $\approx 15 \text{ eV}$ , which is significantly lower than the observed value of  $\approx 100 \text{ eV}$ . Hence we require non-spherical geometry; a larger amount of gas should be present out of the line-of-sight. A possible scenario is that YLW 16A has a disk with face-on geometry (Sekimoto et al. 1997), and this disk is responsible for the fluorescent 6.4 keV line. Since we see no time-lag (reflection time scale) between the flare on-set and the 6.4 keV iron line appearance within  $\lesssim 10^4 \text{ sec}$ , the separation between the star and the reflecting region should be less than  $\lesssim 20 \text{ AU}$ , consistent with the disk origin.

#### 4.8.6. ROX s21 (No.40)

ROX s21, a Class III, has the brightest quiescent flux and exhibits a flare (Figure 10, left panel). Unlike the other sources, a single temperature plasma fit is completely rejected. Thus we add another thin thermal component, and find the fit to be acceptable, allowing the abundance to be free. The best-fit parameters are listed in Table 4. The temperature and flux of the soft component do not change from quiescent to flare, while those of the hard component

increase during the flare (Figure 10, right panel). In fact, if we subtract the quiescent spectrum from that of the flare phase, we obtain a residual 5-keV plasma. We thus suspect that ROX s21 may have fairly steady component with a temperature of 0.84 keV and luminosity of  $7 \times 10^{29} \text{ ergs s}^{-1}$ , and higher temperature plasma arises from frequent flares; a larger one may be recognized as a “flare” (a 5-keV plasma in the present case).

## 5. SUMMARY

A 100-ks observation on the  $\rho$  Oph cloud with *Chandra* revealed the following:

1. We detect 87 X-ray sources from the cloud with a limiting luminosity of  $\sim 10^{28} \text{ ergs s}^{-1}$ .
2. We detect X-rays from 7 Class Is, 11 Class I<sub>c</sub>s. The X-ray detection rates are both  $\sim 70 \%$ .
3. No X-rays are found from starless cores with even younger ages than Class I.
4. We detect X-rays from 1 BD and 1 BD<sub>c</sub>. X-ray properties of these sources are the same as Class II+III<sub>s</sub> of more massive stars.
5. We find 14, 12, 9, and 1 flares from 18 Class I+I<sub>c</sub>s, 20 Class II+III<sub>s</sub>, 17 unclassified sources, and 29 unidentified sources. Thus the duty ratio of flares in Class I+I<sub>c</sub>s is nearly equal to, or slightly higher than that of the other classes. Most of the flares show typical solar-like profiles, a fast rise and slow decay, except for a giant flare from YLW 16A.
6. Most of the X-ray spectra are well fitted with a single temperature thin plasma model of 0.3 solar abundances. In general, Class I+I<sub>c</sub>s have a higher temperature and absorption column than Class II+III<sub>s</sub>.
7. We find that Class I+I<sub>c</sub>s have a systematically smaller  $L_X/L_{\text{bol}}$  value than Class II+III<sub>s</sub>.
8. We derive the empirical relation of  $N_{\text{H}} = 1.26 E(J - H) 10^{22} \text{ cm}^{-2}$  for the cloud members.
9. From the  $kT$ -EM relation obtained by Shibata & Yokoyama (1999), we infer the magnetic field to be 15–500 G, with a hint that Class I+I<sub>c</sub>s have systematically stronger magnetic fields than Class II+III<sub>s</sub>.
10. Luminosity ratios between flare and quiescent phases of Class I+I<sub>c</sub>s are systematically larger than those of Class II+III<sub>s</sub>.
11. We find 29 unidentified sources (no IR/optical counterpart), which are generally hard and heavily absorbed. Most of the unidentified sources are likely

to be background AGNs.

The authors express their thanks to Eric Feigelson, Gordon Garmire, and Yoshitomo Maeda for kind hospitality to the *Chandra* data analysis at PSU. We also thank to Thierry Montmerle, Nicolas Grosso, and Leisa Townsley for useful discussions and comments. A part of this work is supported by the JSPS grant of collaboration with foreign country (grant No. 10147103). YT is financially supported by JSPS.

## REFERENCES

- André, P. & Montmerle, T. 1994, *ApJ*, 420, 837
- Barsony, M., Burton, M. G., Russell, A. P. G., Carlstrom, J. E., & Garden, R. 1989, *ApJ*, 346, L93
- Barsony, M., Kenyon, S. J., Lada, E. A., & Teuben, P. J. 1997, *ApJS*, 112, 109
- Bouvier, J. & Appenzeller, I. 1992, *A&AS*, 92, 481
- Carkner, L., Kozak, J. A., & Feigelson, E. D. 1998, *AJ*, 116, 1933
- Casanova, S., Montmerle, T., Feigelson, E. D., & André, P. 1995, *ApJ*, 439, 752
- Chen, H., Myers, P. C., Ladd, E. F., & Wood, D. O. S. 1995, *ApJ*, 445, 377
- Chen, H., Grenfell, T. G., Myers P. C., & Hughes, J. D. 1997, *ApJ*, 478, 295
- Comerón, F., Rieke, G. H., Burrows. A., & Rieke, M. J. 1993, *ApJ*, 416, 185
- Cox, A. N. 2000, *Allen's astrophysical quantities* (4th ed; New York: AIP Press, Springer)
- Cushing, M. C., Tokunaga, A. T., & Kobayashi, N. 2000, *AJ*, 119, 3019
- Dame. T. M. et al. 1987, *ApJ*, 322, 706
- Elias, J. H. 1978, *ApJ*, 224, 453
- Feigelson, E. D., & DeCampli, W. M. 1981, *ApJ*, 243, L89
- Feigelson, E. D., Casanova, S., Montmerle, T., & Guibert, J. 1993, *ApJ*, 416, 623
- Feldman, U., Laming, J. M., & Doschek, G. A. 1995, *ApJ*, 451, L79
- Festin, L. 1998, *A&A*, 336, 883
- Fleming, T. A., Schmitt, J. H. M. M., & Giampapa, M. S. 1995, *ApJ*, 450, 401
- Greene, T. P. & Young, E. T. 1992, *ApJ*, 395, 516
- Grosso, N., Montmerle, T., Feigelson, E. D., André, P., Casanova, S., & Gregorio-Hetem, J. 1997, *Nature*, 387, 56
- Grosso, N., Montmerle, T., Bontemps, S., André, P., & Feigelson, E. D. 2000, *A&A*, 359, 113
- Grosso, N. 2001, *A&A*, in press (astro-ph/0103013)
- Inoue, H. 1985, *Space Sci. Rev.*, 40, 317
- Kamata, Y., Koyama, K., Tsuboi, Y., & Yamauchi, S. 1997, *PASJ*, 49 461
- Knude, J. & Hog, E. 1998, *A&A*, 338, 897
- Koyama, K., Maeda, Y., Ozaki, M., Ueno, S., Kamata, Y., Tawara, Y., Skinner, S., & Yamauchi, S. 1994, *PASJ*, 46, L125
- Koyama, K., Hamaguchi, K., Ueno, S., Kobayashi, N., & Feigelson, E. D. 1996, *PASJ*, 48, L87
- Luhman, K. L. & Rieke, G. H. 1999, *ApJ*, 525, 440
- Martin, P. G., & Whittet, D. C. B. 1990, *ApJ*, 357, 113
- Montmerle, T., Koch-Miramond, L., Falgarone, E., & Grindlay J., E. 1983, *ApJ*, 269, 182
- Montmerle, T., Grosso, N., Tsuboi, Y., & Koyama, K. 2000, *ApJ*, 532, 1097
- Motte, F., André, P., & Neri, R. 1998, *A&A*, 336, 150
- Mushotzky, R. F., Cowie, L. L., Barger, A. J., & Arnaud, K. A. 2000, *Nature*, 404, 459
- Neuhäuser, R. et al. 1999, *A&A*, 343, 883
- Predehl, P., & Schmitt, J. H. M. M. 1995, *A&A*, 293, 889
- Sekimoto, Y., Tatematsu, K., Umamoto, T., Koyama, K., Tsuboi, Y., Hirano, N., & Yamamoto, S. 1997, *ApJ*, 489, L63
- Shibata, K. & Yokoyama, T. 1999, *ApJ*, 526, L49
- Shimizu, T. 1995, *PASJ*, 47, 251
- Shu, F. H., Adams, F. C., & Lizano, S. 1987, *ARA&A*, 25, 23
- Strom, K. M., Kepner, J., & Strom, S. E. 1995, *ApJ*, 438, 813
- Tachihara, K., Mizuno, A., & Fukui, Y. 2000, *ApJ*, 528, 817
- Townsley, L. K., Broos, P. S., Garmire, G. P., & Nousek, J. A. 2000, *ApJ*, 534, L139
- Tsuboi, Y., Koyama, K., Murakami, H., Hayashi, M., Skinner, S., & Ueno, S. 1998, *ApJ*, 503, 894

- Tsuboi, Y. 1999, PhD thesis, see also ISAS RN 689
- Tsuboi, Y., Imanishi, K., Koyama, K., Grosso, N., & Montmerle, T. 2000, ApJ, 532, 1089
- Vrba, F. J., Strom, K. M., Strom, S. E., & Grasdalen, G. L. 1975, ApJ, 197, 77
- Weisskopf, M. C., O'dell, S. L., & van Speybroeck, L. P. 1996, Proc. SPIE, 2805, 2
- Wilking, B. A. & Lada, C. J. 1983, ApJ, 274, 698
- Wilking, B. A., Lada, C. J., & Young, E. T. 1989, ApJ, 340, 823
- Wilking, B. A., Greene, T. P., & Meyer, M. R. 1999, AJ, 117, 469
- Young, E. T., Lada, C. J., & Wilking, B. A. 1986, ApJ, 304, L45

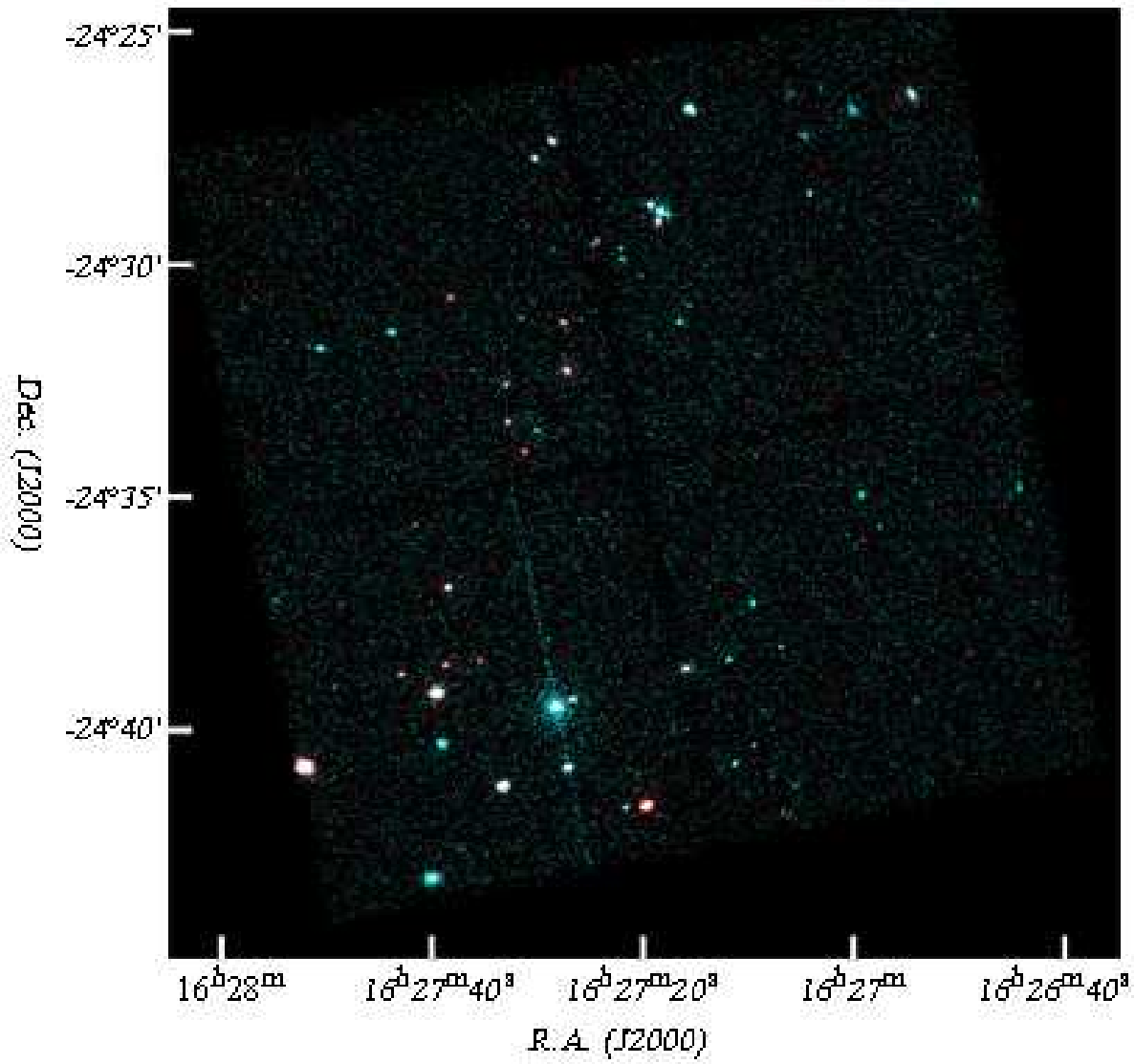


Fig. 1.— ACIS-I image of the  $\rho$  Oph cloud. Red and blue colors represent photons in the soft (0.7–2.0 keV) and hard (2.0–7.0 keV) X-ray bands, respectively.

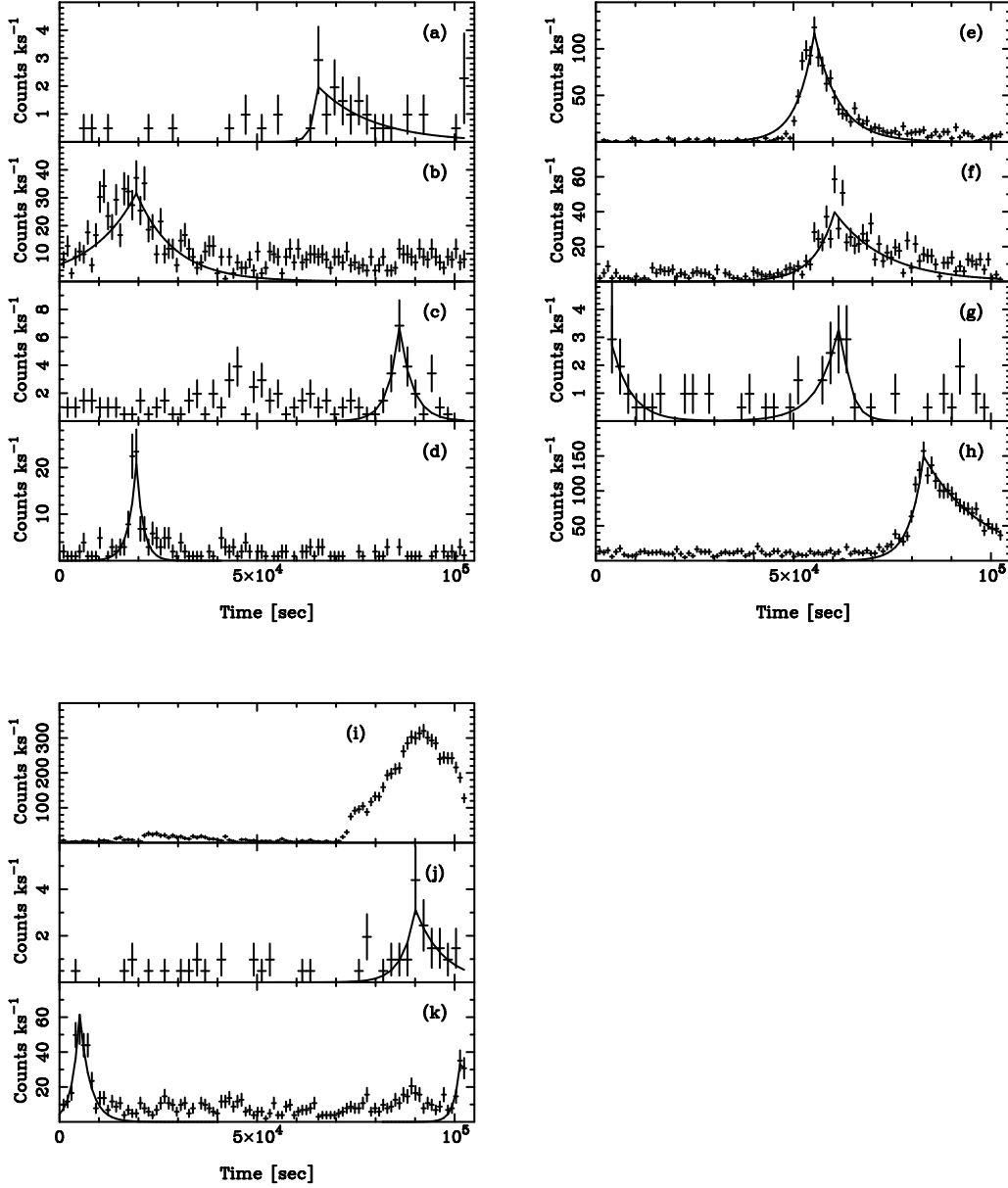


Fig. 2.— Light curves of the flaring Class I+I<sub>cs</sub> in the total (0.7–7.0keV) X-ray band. The horizontal axis is the time from the observation start (MJD = 51647.77) and the vertical axis is the ACIS-I count rate. The best-fit exponential models for the rise and decay phases are shown by solid lines except for (i). The light curve (i) is extracted from  $2''.5-7''.5$  radius in order to avoid the pile-up effect. (a): WL 21 (No.8); (b): EL 29 (No.23); (c): GY 224 (No.24); (d): WL 19 (No.25); (e): YLW 10 (No.26); (f): WL 20 (No.29); (g): GY 256 (No.45); (h): YLW 15A (No.54); (i): YLW 16A (No.57); (j): YLW 16B (No.60); (k): YLW 45 (No.79).

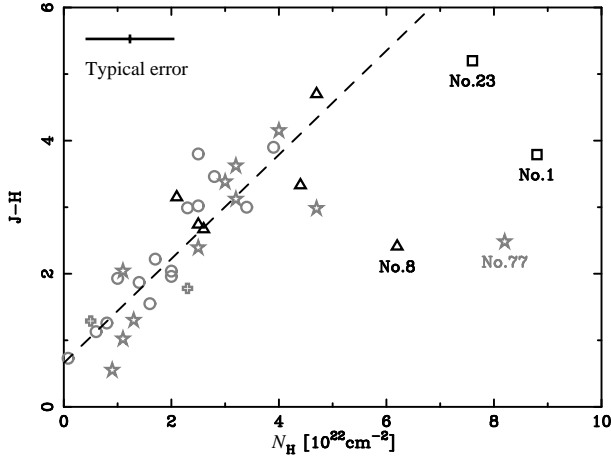


Fig. 3.— Plot of the absorption column ( $N_{\text{H}}$ ) and the near-infrared color ( $J - H$ ). Square, triangle, circle, cross, and star represent Class I, Class I<sub>c</sub>, Class II+III, BD and BD<sub>c</sub>, and unclassified source, respectively. The dashed line represents the best-fit linear model excluding the data points of No.1, 8, 23, and 77.

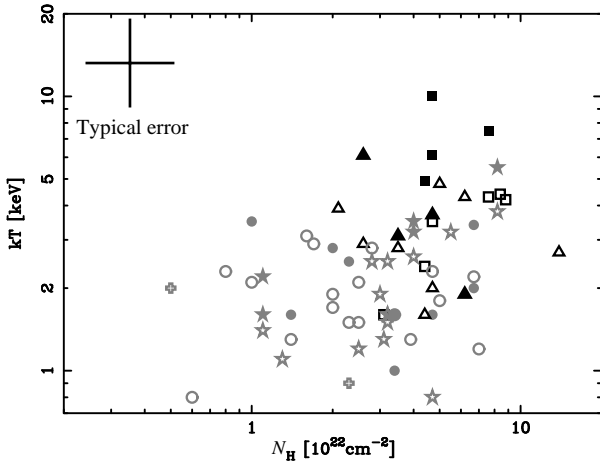


Fig. 4.— Plot of the absorption column density ( $N_{\text{H}}$ ) and the plasma temperature ( $kT$ ). Symbols are the same as Figure 3. For flare sources, those of quiescent and flare phases are separately given by open and filled symbols. Note that the flare and quiescent data of an unclassified source No.77 (GY 312) lie at large  $N_{\text{H}} \approx 8 \times 10^{22} \text{ cm}^{-2}$ , similar to Class Is (see text).

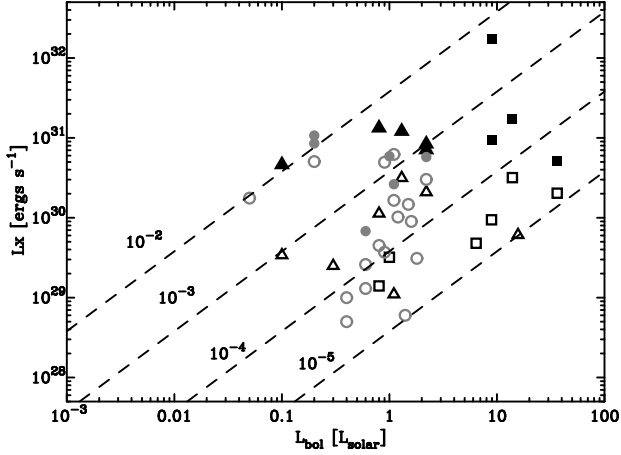


Fig. 5.— Plot of the bolometric luminosity ( $L_{\text{bol}}$ ) and the X-ray luminosity ( $L_X$ ). Symbols are the same as Figure 3. The dashed lines represent the constant  $L_X/L_{\text{bol}}$  ratio of  $10^{-2}$ – $10^{-5}$ .

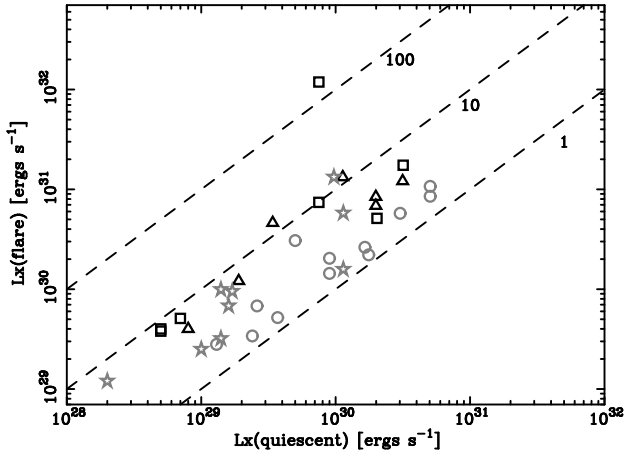


Fig. 6.— Plot of the X-ray luminosity in the quiescent and flare phases. Symbols are the same as Figure 3. Dashed lines represent  $L_x(\text{flare}) = \alpha L_x(\text{quiescent})$  ( $\alpha = 1, 10, 100$ ) relations. An unclassified source No.77 (GY 312) lies at  $\alpha > 10$ , similar to Class Is (see text).

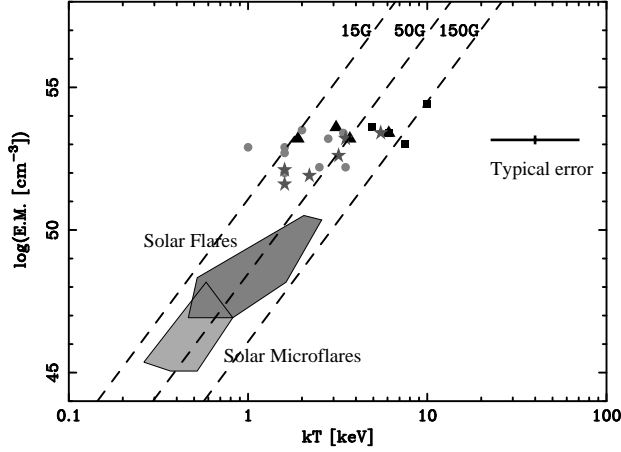


Fig. 7.— Plot of the plasma temperature ( $kT$ ) and the emission measure (EM) in the flare phase. Symbols are the same as Figure 3. The dark and light gray regions represent solar flares and micro flares. The dashed lines are the EM- $kT$  relation ( $EM \propto B^{-5}T^{17/2}$ ) by Shibata & Yokoyama (1999) for  $B = 15, 50, 150$  G. Note that an unclassified source No.77 (GY 312) lies at  $kT = 5-6$  keV, similar to Class Is (see text).

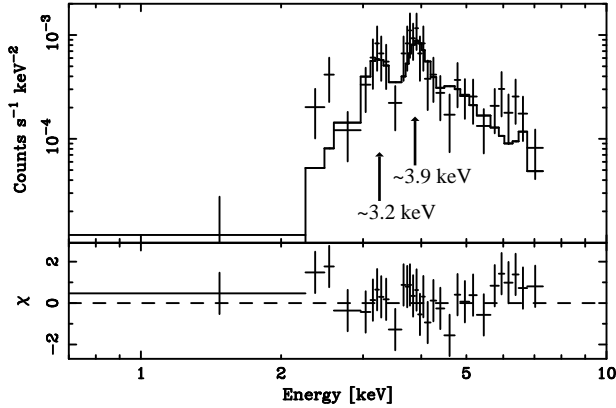


Fig. 8.— Spectrum of WL 22 (No.10). The upper panel shows data points (crosses) and the best-fit thin-thermal plasma model (solid line), while the lower panel shows residuals from the best-fit model. Line structures at  $\sim 3.2$  keV and  $\sim 3.9$  keV are due to He-like Ar and Ca.

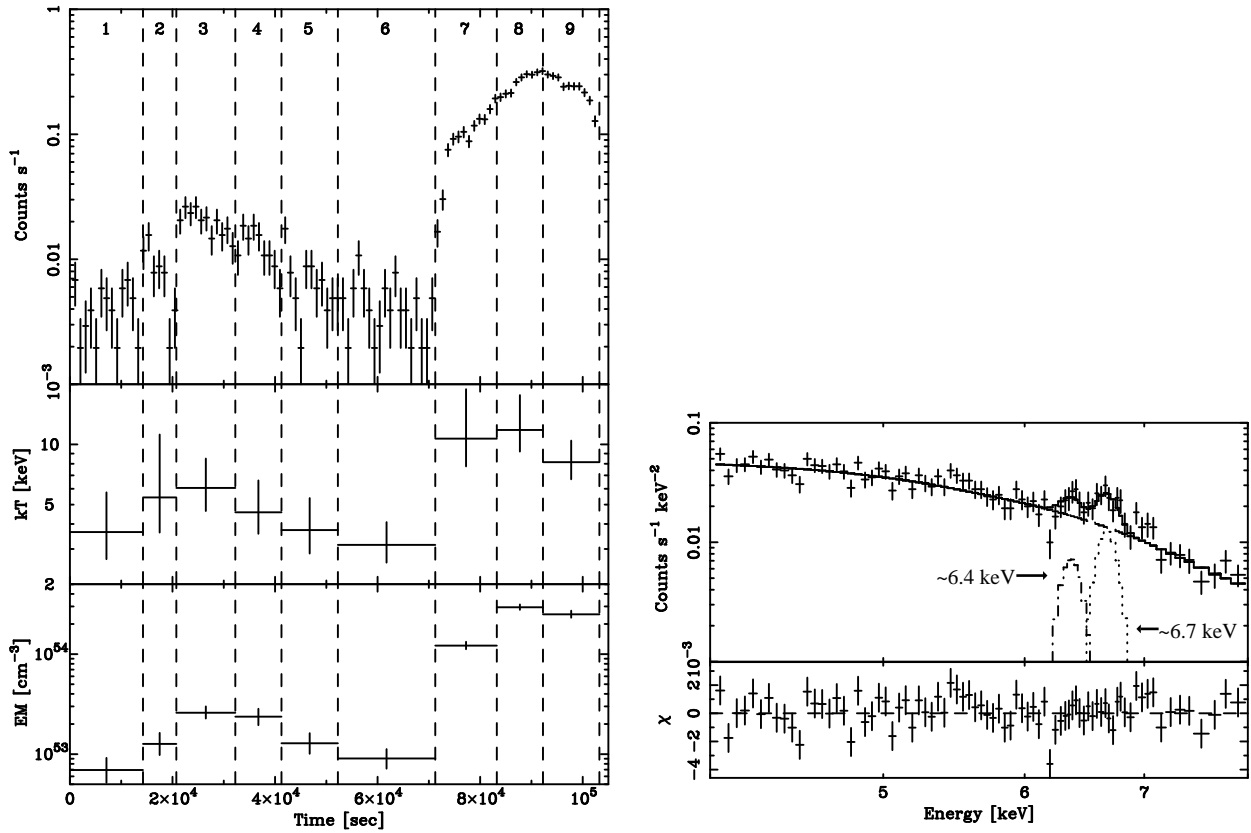


Fig. 9.— (left): Light curve of YLW 16A (No.57, upper) and time profile of the best-fit temperature (middle) and the emission measure (lower). (right): Spectrum of YLW 16A in phases 7–9. The upper panel shows data points (crosses) and the best-fit model (solid line), while the lower panel shows residuals from the best-fit model. Line structures are seen at 6.4 keV and 6.7 keV.

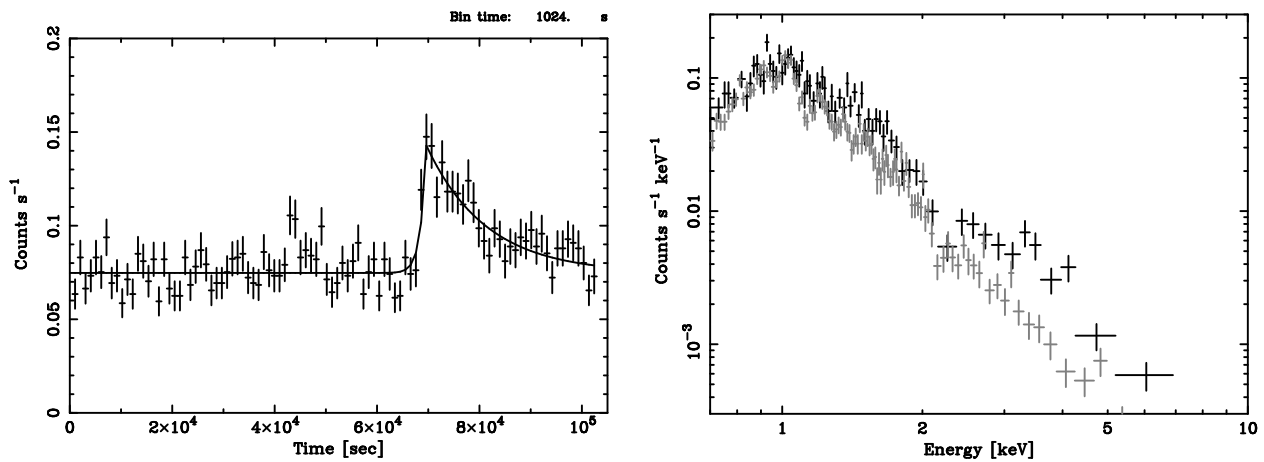


Fig. 10.— (left): Light curve of ROXs 21 (No.40) for the total X-ray band. The solid line represents the best-fit (exponential + constant) model. (right): Spectra of ROXs 21 (No.40) in the flare (black) and quiescent (gray) phases.

TABLE 1  
CHANDRA X-RAY SOURCES IN THE  $\rho$  OPH REGION

No. (1)	R.A. (2)	Dec. (3)	Err (4)	Cts ks <sup>-1</sup> (5)	kT (6)	log(EM) (7)	N <sub>H</sub> (8)	Flux (9)	Lx (10)	Phase (11)
1	16:26:44.2	-24:34:49.5	0.8	1.36	4.2(1.7-76.5)	52.1(51.7-52.7)	8.8(5.9-13.8)	4.4(3.6-5.2)	4.8(2.3-20.2)	
2	16:26:48.6	-24:28:35.3	2.0	0.59	1.2(0.4-4.1)	52.3(51.4-55.0)	7.0(3.4-19.3)	1.0(0.7-1.3)	5.5(>0.7)	
3	16:26:48.9	-24:38:22.8	1.7	0.15	1.8(0.3-55.0)	50.6(50.0-56.7)	0.7(<4.1)	0.2(0.1-0.3)	0.1(>0.03)	
4	16:26:52.0	-24:30:39.5	1.5	0.26	2.0(>0.5)	51.5(50.6-53.8)	6.4(1.7-20.4)	0.5(0.3-0.7)	1.0(0.1-217)	
5 <sup>a</sup>	16:26:52.3	-24:31:33.1	1.4	0.31	1.0(fixed)	53.7(53.3-54.1)	59.0(41.4-83.4)	0.8(0.5-1.1)	141(50.2-317)	
					5.0(fixed)	51.8(51.4-52.1)	31.6(18.3-53.2)	1.3(0.8-1.8)	2.6(1.1-5.1)	
6 <sup>a</sup>	16:26:54.0	-24:39:24.7	1.6	0.17	1.0(fixed)	52.6(52.1-53.3)	21.3(12.4-52.0)	0.3(0.2-0.4)	12.3(3.2-54.2)	
					5.0(fixed)	51.2(50.6-51.6)	12.1(4.3-40.0)	0.6(0.3-0.9)	0.7(0.2-2.0)	
7	16:26:54.4	-24:26:20.5	0.9	4.97	1.5(1.2-1.8)	52.6(52.4-52.7)	2.5(2.2-2.9)	6.5(5.9-7.1)	10.2(7.4-14.4)	
8	16:26:57.3	-24:35:38.7	0.8	0.33	2.9(>0.6)	52.0(51.4-54.4)	6.2(2.3-19.5)	3.4(1.8-5.0)	4.0(1.0-880)	flare
					1.4(>0.4)	51.5(50.5-53.7)	0.3(0.1-0.5)	0.8(0.08-120)	0.5(0.08-120)	quiescent
9	16:26:59.1	-24:35:57.2	0.5	0.37	0.5(0.2-1.6)	52.1(50.9-54.5)	2.5(1.6-4.1)	0.2(0.1-0.3)	3.6(0.2-964)	
10 <sup>c</sup>	16:26:59.2	-24:34:58.6	0.6	1.51	2.7(1.7-5.2)	52.3(51.9-52.8)	13.9(8.4-32.7)	3.5(2.9-4.1)	6.1(2.4-19.3)	
11	16:27:00.0	-24:26:40.4	1.0	2.35	7.8(>2.6)	52.1(52.0-52.6)	8.1(5.7-10.5)	8.6(7.5-9.7)	6.9(4.8-21.4)	
12 <sup>a</sup>	16:27:03.1	-24:26:12.9	2.7	0.07	1.0(fixed)	52.4(51.1-53.0)	17.2(2.6-40.4)	0.3(0.1-0.5)	7.8(0.4-29.6)	
					5.0(fixed)	50.7 <sup>g</sup>	3.8 <sup>g</sup>	0.3(0.1-0.5)	0.2 <sup>g</sup>	
13	16:27:04.1	-24:28:29.3	0.8	0.96	3.9(2.0-13.0)	51.4(51.1-51.7)	2.1(1.2-3.2)	1.6(1.3-1.9)	1.1(0.6-2.3)	
14	16:27:04.5	-24:27:14.9	1.1	1.07	1.6(0.8-6.7)	52.1(51.5-52.7)	3.2(2.1-4.8)	2.0(1.0-3.0)	3.2(0.8-15.6)	flare1
					3.3(>1.3)	52.4(52.1-52.9)	9.4(7.8-16.0)	11.9(7.8-16.0)	9.9(4.6-32.4)	flare2
					1.6(0.9-2.5)	51.7(51.3-52.1)	0.8(0.6-1.0)	1.4(0.5-3.5)	1.4(0.5-3.5)	quiescent
15	16:27:05.3	-24:41:15.0	1.6	0.40	19.4(>1.3)	51.1(50.9-52.6)	5.6(2.8-21.3)	1.3(0.9-1.7)	0.8(0.5-22.2)	
16	16:27:05.9	-24:26:17.5	2.0	0.46	1.3(0.7-9.2)	51.7(50.9-52.5)	3.1(1.3-5.2)	0.5(0.4-0.6)	1.3(0.2-7.9)	
17	16:27:06.6	-24:41:49.8	1.3	0.66	1.6(0.9-5.8)	51.6(51.1-52.1)	1.1(0.2-2.2)	1.3(0.9-1.7)	1.2(0.3-3.8)	flare
					4.6(>0.6)	50.7(50.4-51.5)	0.5(0.3-0.7)	0.5(0.3-0.7)	0.2(0.1-1.3)	quiescent
18	16:27:06.8	-24:38:15.2	0.5	1.10	1.6(1.0-2.7)	52.1(51.6-52.6)	4.4(3.7-6.7)	1.5(1.2-1.8)	3.1(1.1-11.9)	
19 <sup>a</sup>	16:27:07.7	-24:41:04.1	1.8	0.11	1.0(fixed)	52.6(51.8-53.1)	22.2(8.8-43.7)	0.3(0.1-0.5)	11.6(1.6-37.1)	
					5.0(fixed)	51.0(50.1-51.3)	7.6(1.9-25.0)	0.4(0.2-0.6)	0.4(0.07-1.0)	
20 <sup>a</sup>	16:27:08.4	-24:39:39.7	1.4	0.12	1.0(fixed)	53.6(52.5-54.5)	62.9(25.2-132.0)	0.5(0.2-0.8)	102(8.5-942)	
					5.0(fixed)	51.7(50.6-52.6)	36.8(4.1-102.3)	1.0(0.4-1.6)	2.3(0.2-18.4)	
21	16:27:09.1	-24:34:08.2	0.3	0.73	2.9(1.4-12.9)	51.2(50.9-51.6)	1.7(1.3-2.8)	0.8(0.6-1.0)	0.6(0.3-1.6)	
22	16:27:09.3	-24:40:22.1	0.8	0.42	0.8(0.4-1.5)	52.2(51.5-53.4)	4.7(2.9-7.8)	0.5(0.3-0.7)	4.8(0.9-71.8)	
23	16:27:09.4	-24:37:19.0	0.1	11.1	7.5(4.9-16.2)	53.0(52.9-53.1)	7.6(6.8-8.5)	64.4(58.5-70.3)	51.2(41.7-67.9)	flare
					4.3(3.2-6.0)	52.7(52.6-52.8)	2.0(1.8-2.8)	20.2(18.6-21.8)	20.3(15.6-28.1)	quiescent
24 <sup>d</sup>	16:27:11.2	-24:40:46.6	0.8	1.18	>1.9	52.3(52.1-52.5)	5.2(3.6-7.4)	49.2(29.1-69.3)	22.7(13.0-35.1)	flare
					4.5(>2.0)	51.7(51.4-52.1)	2.8(2.2-3.4)	2.8(2.2-3.4)	2.5(1.4-6.9)	quiescent
25	16:27:11.7	-24:38:32.3	0.3	2.13	1.9(1.2-3.6)	53.2(52.8-53.7)	6.2(4.6-8.5)	24.5(18.0-31.0)	46.2(19.2-139.6)	flare
					4.3(2.3-10.7)	51.9(51.7-52.3)	3.7(3.1-4.3)	3.7(3.1-4.3)	3.4(1.9-7.7)	quiescent
26	16:27:15.4	-24:26:39.5	0.4	13.6	3.1(2.6-3.9)	53.6(53.5-53.7)	3.5(3.2-3.9)	148(138-158)	133(109-168)	flare
					2.8(2.3-3.4)	52.5(52.4-52.6)	11.7(10.7-12.7)	11.7(10.7-12.7)	11.3(9.2-14.6)	quiescent
27	16:27:15.5	-24:30:53.7	0.7	0.32	1.8(0.5-27.4)	51.6(50.8-54.0)	5.0(2.2-17.0)	0.6(0.4-0.8)	1.0(0.2-267)	
28	16:27:15.6	-24:33:01.6	0.3	0.40	6.4(>0.4)	51.2(50.9-55.5)	6.3(2.9-52.0)	1.0(0.7-1.3)	0.8(>0.4)	
29	16:27:15.9	-24:38:43.6	0.2	10.4	6.1(3.9-11.3)	53.4(53.3-53.5)	2.6(2.3-3.0)	199(181-217)	121(101-157)	flare
					2.9(2.3-3.6)	52.9(52.8-53.1)	37.3(34.2-40.4)	37.3(34.2-40.4)	31.5(24.9-41.2)	quiescent
30 <sup>d</sup>	16:27:16.4	-24:31:14.7	0.4	1.21	>3.0	52.0(51.8-52.2)	6.9(4.9-10.0)	24.9(15.8-34.0)	11.9(7.4-17.6)	flare
					4.2(>2.0)	51.8(51.5-52.2)	3.0(2.4-3.6)	3.0(2.4-3.6)	3.1(1.6-9.1)	quiescent
31 <sup>d</sup>	16:27:17.0	-24:36:21.5	0.5	0.08	>0.4	49.9(49.0-50.4)	1.0(0.0-16.1)	0.2(0.1-0.3)	0.1(0.01-0.3)	
32 <sup>d</sup>	16:27:17.5	-24:36:27.0	0.5	0.18	>0.6	51.5(50.8-51.9)	23.6(4.4-56.1)	5.3(2.8-7.8)	3.1(0.7-8.4)	
33 <sup>d</sup>	16:27:17.6	-24:28:56.3	0.5	1.15	>1.7	51.8(51.6-52.0)	5.8(4.0-8.8)	13.9(8.4-19.4)	6.5(4.1-9.8)	flare
					7.2(>2.4)	51.7(51.5-52.1)	4.7(3.7-5.7)	4.7(3.7-5.7)	3.2(2.1-9.6)	quiescent
34	16:27:18.2	-24:28:52.4	0.2	18.0	2.0(1.6-2.7)	53.5(53.3-53.6)	6.7(6.2-7.2)	44.5(37.7-51.3)	85.2(56.3-128.6)	flare1
					3.4(2.6-4.7)	53.4(53.3-53.6)	95.6(86.5-105)	95.6(86.5-105)	107(79.8-144)	flare2
					2.2(1.9-2.5)	53.2(53.1-53.3)	30.4(28.7-32.1)	30.4(28.7-32.1)	50.5(40.4-64.5)	quiescent
35 <sup>a</sup>	16:27:18.4	-24:39:14.4	1.0	0.11	1.0(fixed)	52.3(51.7-52.6)	14.7(8.5-27.3)	0.2(0.1-0.3)	5.1(1.4-11.8)	
					5.0(fixed)	50.7(50.1-51.1)	6.2(2.0-20.8)	0.3(0.1-0.5)	0.3(0.07-0.6)	
36	16:27:18.5	-24:29:05.7	0.3	5.49	1.0(0.9-1.2)	52.9(52.7-53.1)	3.4(2.9-3.8)	5.1(4.5-5.7)	20.4(12.7-33.3)	flare1
					1.6(1.3-2.0)	52.7(52.6-52.9)	4.7(2.7-9.2)	8.2(7.2-9.2)	14.4(10.2-20.7)	flare2
					1.6(0.9-5.0)	52.5(52.1-52.9)	5.5(3.0-8.0)	5.5(3.0-8.0)	9.0(3.3-19.9)	quiescent
37 <sup>a</sup>	16:27:19.0	-24:33:44.1	0.5	0.08	1.0(fixed)	51.9(51.1-52.3)	11.5(5.4-26.2)	0.1(0.02-0.2)	2.0(0.4-6.1)	
					5.0(fixed)	50.5(49.8-50.9)	5.0(1.3-17.6)	0.2(0.1-0.3)	0.2(0.04-0.5)	
38	16:27:19.2	-24:28:43.8	0.3	7.14	1.6(1.4-1.9)	52.9(52.7-53.1)	4.7(4.2-5.3)	10.5(9.6-11.4)	22.1(15.2-31.8)	flare
					2.3(1.8-3.1)	52.7(52.6-52.9)	13.1(11.3-14.9)	13.1(11.3-14.9)	17.6(12.6-24.6)	quiescent
39 <sup>d</sup>	16:27:19.3	-24:31:30.7	0.4	0.53	>1.7	51.4(51.2-51.6)	12.7(7.9-21.5)	5.6(4.1-7.1)	2.9(1.8-4.6)	
40	16:27:19.5	-24:41:40.6	0.1	83.8	...	...	see table 4	...	...	
41 <sup>b</sup>	16:27:19.9	-24:35:31.9	0.8	0.06	...	...	...	...	...	
42	16:27:20.0	-24:30:13.6	0.6	0.14	5.6(>0.3)	51.1(50.5-56.5)	13.8(3.5-82.2)	0.5(0.2-0.8)	0.6(>0.1)	
43	16:27:21.4	-24:41:43.2	0.9	1.39	1.3(0.9-2.0)	52.2(51.8-52.6)	3.9(2.7-5.2)	1.7(1.4-2.0)	4.5(1.9-11.5)	
44	16:27:21.8	-24:29:53.4	0.5	1.21	4.4(2.0-11.8)	51.9(51.6-52.4)	8.4(6.1-12.7)	3.1(2.5-3.7)	3.2(1.7-10.1)	
45	16:27:22.0	-24:29:39.6	0.8	0.56	1.1(>0.8)	52.0(51.5-53.0)	3.1(1.3-5.8)	5.4(2.0-8.8)	4.0(1.5-46.7)	flare1
					2.9(>0.7)	52.0(51.6-53.1)	4.3(2.4-6.2)	4.3(2.4-6.2)	3.8(1.3-47.6)	flare2
					1.6(0.5-40.3)	51.3(50.5-52.5)	0.3(0.2-0.4)	0.3(0.2-0.4)	0.5(0.08-9.0)	quiescent
46 <sup>b</sup>	16:27:22.6	-24:34:15.1	0.4	0.04	...	...	...	...	...	
47	16:27:23.6	-24:31:57.0	0.6	0.17	1.2(>0.2)	53.2(50.9-55.6)	67.6(15.2-156.7)	0.6(0.3-0.9)	42.6(>0.2)	
48	16:27:24.2	-24:29:29.4	0.7	0.52	3.6 <sup>g</sup>	52.4(<55.7)	1.8(0.8-4.4)	14.5(<35.0)	9.5(>0.0)	flare
					8.1(>1.5)	51.5(51.3-52.2)	...	3.3(2.3-4.3)	1.7(1.0-8.9)	quiescent
49 <sup>a</sup>	16:27:24.4	-24:41:49.4	1.9	0.11	1.0(fixed)	51.2(49.9-51.7)	3.0(0.7-7.9)	0.1(0.04-0.2)	0.5(0.02-1.5)	
					5.0(fixed)	50.2 <sup>g</sup>	1.0 <sup>g</sup>	0.1(0.04-0.2)	0.1 <sup>g</sup>	
50	16:27:24.6	-24:29:35.3	0.7	0.65	2.5(1.1-10.7)	51.7(51.2-52.5)	2.8(1.3-5.2)	1.9(1.4-2.4)	1.8(0.6-9.4)	
51 <sup>b</sup>	16:27:25.0	-24:34:35.3	0.6	0.04	...	...	...	...	...	
52 <sup>e</sup>	16:27:26.4	-24:25:55.6	2.1	0.14	0.1(0.04-0.3)	52.9(50.1-58.7)	0.9(0.3-1.9)	0.1(0.05-0.2)	16.6(>0.02)	
53 <sup>d</sup>	16:27:26.5	-24:39:23.1	0.3	5.94	>6.9	52.7(52.7-52.8)	2.8(2.5-3.2)	136(120-152)	58.9(51.9-66.0)	flare
					2.7(2.2-3.6)	52.2(52.1-52.3)	6.0(5.3-6.7)	6.0(5.3-6.7)	6.6(5.0-8.6)	quiescent
					4.9(4.2-6.2)	53.6(53.5-53.6)	4.4(4.1-4.7)	228(217-239)	174(151-198)	flare
54	16:27:27.0	-24:40:50.9	0.2	29.2	2.4(2.1-2.8)	53.0(52.9-53.1)	...	26.5(25.0-28.0)	31.8(26.4-38.1)	quiescent
					3.2(2.3-5.9)	52.6(52.5-52.8)	4.0(3.5-4.5)	17.1(14.2-20.0)	15.8(10.8-22.8)	flare1
					3.5(2.9-4.8)	53.2(53.0-53.2)	...	66.0(60.2-71.8)	57.8(43.6-65.1)	flare2
					2.6(2.1-3.3)	52.5(52.4-52.7)	...	10.5(9.5-11.5)	11.4(8.2-15.4)	quiescent
56	16:27:27.4	-24:31:16.4	0.2	4.86	3.5(2.4-5.0)	52.2(52.1-52.4)	1.0(0.8-1.3)	12.0(10.0-14.0)	6.8(5.1-9.6)	flare
					2.1(1.6-2.8)	51.9(51.8-52.1)	...	3.7(3.3-4.1)	2.6(2.0-3.5)	quiescent
57	16:27:28.0	-24:39:33.5	0.1	188 <sup>f</sup>	...	...	see table 3	...	...	
58	16:27:28.5	-24:29:42.0	0.9	0.24	5.9(>0.8)	51.1(50.7-53.1)	6.3(2.7-22.4)	0.8(0.5-1.1)	0.6(0.3-54.0)	
59	16:27:28.5	-24:27:20.6	0.7	3.06	2.5(1.7-4.2)	52.2(52.0-52.4)	2.3(1.8-2.8)	5.9(4.7-7.1)	5.2(3.3-8.0)	flare

TABLE 1—*Continued*

No. (1)	R.A. (2)	Dec. (3)	Err (4)	Cts ks <sup>-1</sup> (5)	kT (6)	log(EM) (7)	N <sub>H</sub> (8)	Flux (9)	Lx (10)	Phase (11)
					3.2(1.5–23.2)	51.6(51.3–52.2)		1.6(1.2–2.0)	1.9(0.9–6.5)	quiescent
62 <sup>d</sup>	16:27:30.1	–24:38:03.4	0.9	0.11	>0.5	50.3(49.3–50.8)	2.1(<21.1)	0.5(0.2–0.8)	0.2(0.02–0.6)	
63	16:27:30.1	–24:27:43.5	0.8	2.31	2.1(1.3–3.6)	52.0(51.7–52.4)	2.5(1.8–3.8)	3.0(2.6–3.4)	3.1(1.6–8.2)	
64	16:27:31.1	–24:34:03.3	0.3	2.00	2.2(1.1–6.4)	51.9(51.7–52.2)	1.1(0.8–1.7)	3.6(2.7–4.5)	2.5(1.4–5.1)	flare
					1.4(1.0–2.2)	51.6(51.3–51.9)		1.0(0.8–1.2)	1.0(0.6–2.4)	quiescent
65	16:27:31.3	–24:31:10.1	0.5	0.73	7.0(>2.1)	51.4(51.2–52.0)	5.6(3.4–10.3)	1.9(1.5–2.3)	1.4(0.8–5.8)	
66	16:27:32.7	–24:33:24.2	0.2	3.57	2.5(1.8–3.7)	52.2(52.1–52.5)	3.2(2.6–3.9)	5.7(5.1–6.3)	5.8(3.7–9.6)	
67	16:27:32.9	–24:32:35.0	0.3	1.85	1.9(1.3–2.6)	52.0(51.7–52.3)	3.0(2.3–4.0)	2.2(1.9–2.5)	2.8(1.6–5.8)	
68	16:27:33.0	–24:31:48.2	1.4	0.14	1.9(>0.1)	51.2(50.0–62.5)	7.4(1.0–27.5)	0.2(0.1–0.3)	0.5(>0.03)	
69	16:27:33.1	–24:41:15.3	0.2	31.3	2.8(2.5–3.3)	53.2(53.1–53.3)	2.0(1.9–2.1)	74.6(70.5–78.7)	57.6(49.4–64.2)	flare
					1.9(1.8–2.2)	53.0(52.9–53.1)		29.6(28.2–31.0)	30.2(25.5–33.1)	quiescent
70	16:27:35.3	–24:38:33.7	0.7	1.03	0.8(0.6–1.1)	51.2(51.0–51.5)	0.6(0.4–0.9)	0.4(0.3–0.5)	0.5(0.3–0.9)	
71 <sup>d</sup>	16:27:36.0	–24:32:18.4	1.0	0.26	>3.0	50.7(50.4–51.0)	2.1(0.8–6.7)	1.4(0.9–2.0)	0.6(0.3–1.1)	
72	16:27:37.3	–24:42:38.5	2.4	0.16	1.5(0.4–15.4)	51.4(50.5–53.6)	3.2(0.7–14.1)	0.4(0.2–0.6)	0.7(0.09–99.6)	
73	16:27:37.6	–24:36:04.4	1.1	0.27	5.3(>0.5)	50.8(50.3–53.2)	3.3(0.8–14.0)	0.4(0.3–0.6)	0.3(0.1–71.4)	
74	16:27:38.2	–24:30:42.6	0.6	1.71	1.6(1.0–2.7)	52.0(51.8–52.4)	1.4(1.1–2.1)	2.7(2.1–3.3)	2.8(1.7–6.4)	flare
					1.3(0.9–2.0)	51.7(51.4–52.0)		1.0(0.8–1.2)	1.3(0.7–2.9)	quiescent
75	16:27:38.3	–24:36:58.4	0.2	12.3	1.7(1.5–1.9)	52.7(52.6–52.8)	2.0(1.8–2.2)	12.5(11.8–13.2)	14.7(12.1–17.5)	
76	16:27:38.6	–24:38:39.1	0.5	2.83	2.0(1.5–2.5)	51.5(51.4–51.6)	0.5(0.3–0.7)	1.9(1.7–2.1)	1.0(0.8–1.3)	
77	16:27:39.0	–24:40:20.5	0.4	7.38	5.5(3.2–11.2)	53.4(53.3–53.7)	8.2(6.9–10.1)	144(130–158)	133.0(93.5–223.6)	flare
					3.8(2.5–7.1)	52.4(52.2–52.6)		8.5(7.6–9.5)	9.7(5.9–17.5)	quiescent
78	16:27:39.5	–24:39:15.5	0.1	66.7	3.1(2.9–3.4)	53.2(53.2–53.3)	1.6(1.5–1.6)	92.4(90.1–94.7)	62.1(57.7–66.7)	
79 <sup>d</sup>	16:27:39.9	–24:43:15.3	0.7	9.36	>10.6	53.2(53.1–53.2)	4.8(4.3–5.5)	143(122–163)	83.9(71.6–96.8)	flare1
					3.5(2.0–13.0)	53.3(53.0–53.5)		74.4(55.8–93.0)	71.0(38.7–124.9)	flare2
					1.9(1.6–2.3)	52.9(52.7–53.0)		12.5(11.6–13.5)	20.9(15.3–28.9)	quiescent
80	16:27:41.5	–24:35:37.7	0.9	0.54	1.2(0.5–2.8)	51.6(51.0–52.7)	2.5(1.4–4.2)	0.5(0.4–0.6)	1.0(0.3–14.4)	
81	16:27:42.8	–24:38:51.1	0.8	1.45	0.9(0.6–1.2)	52.1(51.7–52.6)	2.3(1.6–3.2)	1.0(0.8–1.2)	3.8(1.5–12.0)	
82 <sup>d</sup>	16:27:43.7	–24:31:26.6	0.6	2.49	>5.5	51.9(51.8–52.0)	5.2(4.4–6.5)	19.3(16.9–21.8)	8.9(7.6–10.4)	
83 <sup>d</sup>	16:27:49.1	–24:39:06.9	1.7	0.29	>0.4	50.9(50.3–51.3)	4.4(0.5–17.7)	2.1(1.3–2.9)	1.0(0.3–2.4)	
84	16:27:50.4	–24:31:49.3	1.0	1.64	2.8(1.2–7.5)	52.1(51.6–53.1)	6.4(3.9–15.4)	3.2(2.7–3.7)	4.0(1.5–42.9)	
85	16:27:52.0	–24:40:50.0	0.3	46.3	2.3(2.2–2.4)	53.2(53.2–53.2)	0.8(0.7–0.8)	81.3(78.9–83.7)	49.5(46.9–52.9)	
86 <sup>a</sup>	16:27:54.7	–24:37:14.9	1.9	0.50	1.0(fixed)	52.7(52.4–53.0)	14.2(9.8–21.8)	0.8(0.6–1.0)	15.7(7.3–30.8)	
					5.0(fixed)	51.4(51.1–51.6)	6.6(3.8–12.0)	1.2(0.9–1.5)	1.1(0.6–1.8)	
87	16:27:55.3	–24:28:39.4	2.2	0.28	1.1(0.1–3.7)	51.2(50.6–56.4)	1.3(0.2–4.0)	0.3(0.2–0.4)	0.5(>0.1)	

NOTE.— (1): Source number. (2),(3): Source coordinate in the equinox 2000. (4): Position uncertainty [arc-sec] with the 90% confidence limit. (5): Photon counts ks<sup>-1</sup>. (6),(7),(8),(9),(10): Plasma temperature [keV], log(Emission Measure [cm<sup>-3</sup>]), absorption column density [10<sup>22</sup> cm<sup>-2</sup>], observed flux [10<sup>-14</sup> ergs s<sup>-1</sup> cm<sup>-2</sup>] in 0.5–10.0 keV, and absorption-corrected luminosity [10<sup>29</sup> ergs s<sup>-1</sup>] in 0.5–10.0 keV, respectively. Parentheses indicate the 90% confidence limits. (11): Phases for the spectral fit. Flare 1 and 2 indicate 2 flares, which are separately treated (see text).

<sup>a</sup>Spectral parameters are obtained with fixed temperatures of 1 keV and 5 keV (see text).

<sup>b</sup>No spectral fit is done due to limited flux (<0.06 cts ks<sup>-1</sup>).

<sup>c</sup>Abundances are free parameters (see §4.8.1 and Figure 8).

<sup>d</sup>The best-fit value of kT is not determined (larger than 20 keV), hence we assume 20 keV temperature for the estimation of the other parameters.

<sup>e</sup>Foreground star. The distance is assumed to be 60 pc (Festin 1998).

<sup>f</sup>File-up effect is not corrected.

<sup>g</sup>Errors are not constrained.

TABLE 2  
IDENTIFICATIONS OF THE X-RAY SOURCES

No. (1)	BKLT (2)	PSPC (3)	HRI (4)	ASCA (5)	Other names (6)	Class (7)	$L_{bol}$ (8)	Reference Class	$L_{bol}$
1	162644-243447	...	...	...	WL12/YLW2/GY111/VSSG30/BBRCG4	I	6.4	1,2,3,4,5	3
2	162648-242836	...	...	...	WL2/GY128/BBRCG6	II	...	1	
3	...	...	...	...	...	...	...	...	
4	...	...	...	...	...	...	...	...	
5	...	...	...	...	...	...	...	...	
6	...	...	...	...	...	...	...	...	
7	162654-242622	33	...	...	VSSG5/GY153	II	1.2	1	5
8	162657-243538	34	...	...	WL21/IRS23/GY164/BBRCG/17/CRBR50/SKS3-23	I <sub>c</sub>	0.0	4	6
9	162659-243556	...	...	...	WL14/GY172/BBRCG18/CRBR52/SKS3-25	I <sub>c</sub>	...	4	
10	162659-243458	...	...	...	WL22/IRS27/GY174/CRBR53	I <sub>c</sub>	15.7	3,4	3
11	...	...	...	...	...	...	...	...	
12	162703-242615	...	...	...	GY188	?	...	...	
13	162704-242830	...	...	...	WL1/IRS29/GY192/VSSG31/BBRCG20/CRBR55	I <sub>c</sub>	1.1	3	3
14	162704-242716	...	...	...	GY195	?	...	...	
15	...	...	...	...	...	...	...	...	
16	162705-242619	...	...	...	GY203/IRS30	?	...	...	
17	162706-244147	...	...	...	GY204/SKS1-26	?	...	...	
18	162706-243814	...	...	C5	WL17/GY205/BBRCG22/CRBR58/SKS3-27	I <sub>c</sub>	...	5	
19	...	...	...	...	...	...	...	...	
20	...	...	...	...	...	...	...	...	
21	162709-243408	37	...	7	WL10/GY211/BBRCG24/CRBR59/SKS1-27	II	1.4	2	5
22	162709-244022	...	...	...	GY213/SKS3-28	?	...	...	
23	162709-243718	...	...	8	EL29/YLW7/GY214/BBRCG23/CRBR60/SKS1-28	I	36.3	1,2,3,4,5	3
24	162711-244046	...	...	...	GY224/SKS3-30	I <sub>c</sub>	0.3	2,4,5	3
25	162711-243832	...	...	...	WL19/YLW11/GY227/BBRCG28/CRBR65/SKS3-31	I <sub>c</sub>	0.1	5,6	6
26	162715-242640	...	...	...	IRS34/YLW10/GY239/SKS3-36	I <sub>c</sub>	0.8	3	3
27	162715-243054	...	F15	...	GY238/BBRCG32/CRBR70/SKS3-35/IRS35	II	0.4	7	7
28	...	...	...	...	...	...	...	...	
29	162715-243843	39	F16	...	WL20/GY240/BBRCG31/CRBR68/SKS1-31	I <sub>c</sub>	1.3	1,4	7
30	...	...	...	...	...	...	...	...	
31	...	...	...	...	...	...	...	...	
32	...	...	...	...	...	...	...	...	
33	162717-242856	...	...	...	IRS37/YLW12A/GY244/VSSG26/BBRCG36/CRBR71/SKS1-32	II?	...	2	
34	162718-242853	40	...	...	WL5/IRS38/GY246/VSSG26/BBRCG37/CRBR73/SKS1-33	III	0.2	2	3
35	162718-243915	...	...	...	GY245/BBRCG39/CRBR72/SKS3-37	I <sub>c</sub>	0.1	2,4	3
36	162718-242906	...	...	C6	WL4/IRS39/GY247/VSSG26/BBRCG40/CRBR75/SKS1-34	II	1.6	1	5
37	...	...	...	...	...	...	...	...	
38	162719-242844	...	...	...	WL3/IRS41/GY249/VSSG26/CRBR77/SKS3-38	II	0.05	1	6
39	...	...	...	...	...	...	...	...	
40	162719-244139	41	F17	9A	SR12AB/ROXs21/GY250/CRBR76/SKS1-35/IRS40	III	1.1	1	7
41	...	...	...	...	...	...	...	...	
42	...	...	...	...	...	...	...	...	
43	162721-244142	...	...	...	IRS42/YLW13B/GY252/CRBR79/SKS1-36	II	0.8	1	6
44	162721-242953	...	...	10	WL6/YLW14/GY254/CRBR80/SKS3-40	I	1.0	1,2,4,5,6	6
45	162722-242939	...	...	...	GY256/BBRCG43/CRBR81/SKS3-41	I	...	2	
46	...	...	...	...	...	...	...	...	
47	...	...	...	...	...	...	...	...	
48	162724-242929	...	...	...	GY257/CRBR83/SKS3-43	?	...	...	
49	162724-244147	...	...	...	GY258/CRBR84/SKS3-42	?	...	...	
50	162724-242935	...	...	...	GY259/CRBR86/SKS3-45	?	...	...	
51	...	...	...	...	...	...	...	...	
52	162726-242555	...	...	...	GY264/SKS1-37	F	...	8	
53	162726-243923	...	...	...	GY262/BBRCG45/CRBR88/SKS3-47	II	1.0	2	5
54	162726-244051	43	F21	T <sup>a</sup>	IRS43/YLW15A/GY265/CRBR89/SKS3-49	I	13.9	1,2,3,4,5	7
55	162727-243217	...	...	...	GY266/SKS3-5	?	...	...	
56	162727-243116	44	F22	...	VSSG25/WL13/GY267/VSSG25/EL31/SKS1-38	II	0.6	1	7
57	162728-243934	45	G <sup>b</sup>	...	IRS44/YLW16A/GY269/BBRCG49/SKS3-51	I	8.9	1,2,3,4,5	3
58	...	...	...	...	...	...	...	...	
59	162728-242721	...	...	...	VSSG18/IRS45/GY273/VSSG18/EL32/SKS1-39	II	0.9	1	5
60	162729-243917	...	...	9B	IRS46/YLW16B/GY274/BBRCG52/SKS3-54	I	0.8	1,2,3,4,5	3
61	162730-243336	...	...	...	...	?	...	...	
62	...	...	...	...	...	...	...	...	
63	162730-242744	...	...	...	VSSG17/IRS47/GY279/EL33/SKS1-40	II	1.8	1	5
64	162731-243402	47	...	...	GY283/BBRCG56	?	...	...	
65	...	...	...	...	...	...	...	...	
66	162732-243323	...	...	...	GY289/BBRCG60	?	...	...	
67	162732-243235	48?	...	...	GY291/BBRCG61	?	...	...	
68	...	...	...	...	...	...	...	...	
69	162733-241115	49	F27	...	GY292/CRBR90	II	2.2	2	7
70	162735-243834	...	...	...	GY295/SKS1-44	III	0.4	5	5
71	...	...	...	...	...	...	...	...	
72	162737-244238	...	...	...	GY301/SKS3-59	?	...	...	
73	...	...	...	...	...	...	...	...	
74	162738-243043	...	...	...	IRS50/GY306/SKS1-47	III	0.6	1	5
75	162738-243658	50	F29	...	IRS49/GY308/SKS1-48	III	1.5	5	7
76	162738-243838	...	...	...	GY310/SKS1-49	BD	0.08	9	5
77	162738-244019	...	...	...	GY312/SKS3-61	?	...	...	
78	162739-243914	51	F30	...	GY314/SKS1-50	II	1.1	2	7
79	162739-244316	...	...	T <sup>a</sup>	IRS51/YLW45/GY315/SKS3-63	I <sub>c</sub>	2.2	1,2,3,4	3
80	162741-243537	...	...	...	GY322	?	...	...	
81	162742-243849	...	...	...	GY326/SKS1-52	BD <sub>c</sub>	0.4	9	5

TABLE 2—*Continued*

No. (1)	BKLT (2)	PSPC (3)	HRI (4)	ASCA (5)	Other names (6)	Class (7)	$L_{\text{bol}}$ (8)	Reference Class	$L_{\text{bol}}$
82	...	...	...	...	...	...	...		
83	...	...	...	...	...	...	...		
84	...	...	...	...	...	...	...		
85	162752–244049	54	G <sup>b</sup>	T <sup>a</sup>	ROXs31/IRS55/GY380	III	0.9	1	3
86	...	...	...	...	...	...	...		
87	162755–242840	...	...	...	GY397	?	...		

NOTE.— (1): Source number. (2): *JHK* band counterpart (Barsony et al. 1997). (3): *ROSAT* PSPC sources (Casanova et al. 1995). (4): *ROSAT* HRI sources (Grosso et al. 2000). (5): *ASCA* sources (Kamata et al. 1997). (6): Abbreviations: BBRCG (Barsony et al. 1989), CRBR (Comerón et al. 1993), EL (Elias 1978), GY (Greene & Young 1992), IRS (Wilking, Lada, & Young 1989), ROXs (Bouvier & Appenzeller 1992), SKS (Strom, Kepner, & Strom 1995), VSSG (Vrba et al. 1975), WL (Wilking & Lada 1983), YLW (Young, Lada, & Wilking 1986). (7): Classifications: I: Class I, I<sub>c</sub>: Class I candidate, II: Class II, III: Class III, BD: brown dwarf, BD<sub>c</sub>: brown dwarf candidate, F: foreground star. Unclassified sources are indicated by question mark (?). (8): Bolometric luminosity [ $L_{\odot}$ ] assuming 165 pc distance.

<sup>a</sup>Tsuboi et al. (2000)

<sup>b</sup>Grosso (2001)

REFERENCES.— (1) André & Montmerle 1994; (2) Casanova et al. 1995; (3) Chen et al. 1995; (4) Motte, André, & Neri 1998; (5) Luhman & Rieke 1999; (6) Chen et al. 1997; (7) Grosso et al. 2000; (8) Festin 1998; (9) Wilking, Greene, & Meyer 1999.

TABLE 3  
BEST-FIT PARAMETERS OF YLW 16A (No.57)

Phase <sup>a</sup>	$kT$ [keV]	$\log(\text{EM})$ [ $\text{cm}^{-3}$ ]	$N_{\text{H}}^{\text{b}}$ [ $10^{22}\text{cm}^{-2}$ ]	EW <sup>c</sup> [eV]	Flux <sup>d</sup> [ $10^{-12}\text{ergs s}^{-1}\text{cm}^{-2}$ ]	$Lx^{\text{e}}$ [ $10^{31}\text{ergs s}^{-1}$ ]
1	3.6(2.7–5.8)	52.8(52.7–53.0)	4.7(4.5–4.8)	...	0.3(0.3–0.3)	0.3(0.2–0.4)
2	5.4(3.6–11.2)	53.1(53.0–53.2)	4.7	...	0.8(0.7–0.9)	0.6(0.5–0.8)
3	6.1(4.6–8.5)	53.4(53.4–53.5)	4.7	...	1.8(1.7–1.9)	1.3(1.1–1.5)
4	4.6(3.6–6.6)	53.4(53.3–53.5)	4.7	...	1.3(1.2–1.4)	1.1(0.9–1.3)
5	3.7(2.8–5.4)	53.1(53.0–53.2)	4.7	...	0.6(0.5–0.7)	0.5(0.4–0.6)
6	3.1(2.6–4.1)	53.0(52.9–53.1)	4.7	...	0.3(0.3–0.3)	0.3(0.2–0.4)
7	10.7(7.8–18.9)	54.1(54.0–54.1)	4.7	146(44–248)	10.9(10.3–11.5)	6.8(6.3–7.4)
8	11.8(9.2–17.6)	54.5(54.4–54.5)	4.7	95(23–167)	26.9(25.8–28.0)	16.7(15.7–17.8)
9	8.1(6.7–10.4)	54.4(54.4–54.4)	4.7	92(25–160)	20.1(19.3–20.9)	13.3(12.3–14.5)

<sup>a</sup>See Figure 9.

<sup>b</sup> $N_{\text{H}}$  is assumed to be the same value in all the phases.

<sup>c</sup>Equivalent width for the 6.4 keV line.

<sup>d</sup>Observed flux in 0.5–10.0 keV.

<sup>e</sup>Absorption-corrected luminosity in 0.5–10.0 keV.

TABLE 4  
BEST FIT PARAMETERS OF ROXs 21 (No.40) FOR THE (THIN-THERMAL + THIN-THERMAL) MODEL

		$kT$ [keV]	$\log(\text{EM})$ [ $\text{cm}^{-3}$ ]	Abundance <sup>a</sup> [solar]	$N_{\text{H}}^{\text{a}}$ [ $10^{22}\text{cm}^{-2}$ ]	Flux <sup>b</sup> [ $10^{-14}\text{ergs s}^{-1}\text{cm}^{-2}$ ]	$Lx^{\text{c}}$ [ $10^{29}\text{ergs s}^{-1}$ ]
flare	soft	0.84(0.76–1.04)	52.5(52.3–52.6)	0.19(0.16–0.24)	0.08(0.04–0.12)	17.5(16.1–18.9)	7.2(4.9–9.6)
	hard	2.49(2.07–2.89)	52.8(52.7–52.9)	0.19	0.08	51.9(48.9–54.9)	19.1(17.2–22.3)
quiescent	soft	0.83(0.78–0.88)	52.5(52.4–52.6)	0.19	0.08	17.9(17.2–18.6)	7.3(5.5–9.8)
	hard	1.67(1.54–1.85)	52.6(52.5–52.6)	0.19	0.08	24.3(23.4–25.2)	9.2(7.9–9.9)

<sup>a</sup>Abundance and  $N_{\text{H}}$  are assumed to be the same values in all the phases and components.

<sup>b</sup>Observed flux in 0.5–10.0 keV.

<sup>c</sup>Absorption-corrected luminosity in 0.5–10.0 keV.